



Analysis of mild ignition in a shock tube using a highly resolved 3D-LES and high-order shock-capturing schemes

J. T. Lipkowitz¹ · I. Wlokas¹ · A. M. Kempf¹

Received: 18 May 2018 / Revised: 17 September 2018 / Accepted: 20 September 2018 / Published online: 6 October 2018
© Springer-Verlag GmbH Germany, part of Springer Nature 2018

Abstract

A highly resolved three-dimensional large-eddy simulation (LES) is presented for a shock tube containing a stoichiometric hydrogen–oxygen (H_2/O_2) mixture, and the results are compared against experimental results. A parametric study is conducted to test the effects of grid resolution, numerical scheme, and initial conditions before the 3D simulations are presented in detail. An approximate Riemann solver and a high-order interpolation scheme are used to solve the conservation equations of the viscous, compressible fluid and to account for turbulence behind the reflected shock. Chemical source terms are calculated by a finite-rate model. Simultaneous results of pseudo-Schlieren, temperature, pressure, and species are presented. The ignition delay time is predicted in agreement with the experiments by the three-dimensional simulations. The mechanism of mild ignition is analysed by Lagrangian tracer particles, tracking temperature histories of material particles. We observed strongly increased temperatures in the core region away from the end wall, explaining the very early occurrence of mild ignition in this case.

Keywords Large-eddy simulations (LES) · Mild ignition · Shock tube · Tracer particles · Bifurcation

1 Introduction

1.1 Motivation

Shock-tube experiments are a classical technique to provide data for the development of accurate reaction mechanisms. A shock tube consists of a driver section with a pressurized (inert) gas and separated by a diaphragm, at lower pressure, the section filled with the test gas. At a sufficiently high pressure difference between the sections, the diaphragm bursts and a compression shock propagates into the test gas, followed by the contact discontinuity between the mixtures. After the reflection of the shock at the end wall, the temperature of the test gas is increased further by the reflected shock,

initiating the chemical reactions, and an auto-ignition delay time can be measured. Ideally, the test gas behind the reflected shock is at rest and homogeneous, under the assumption of an inviscid, adiabatic process. In reality, deviations from the ideal assumptions affect the system and hence the measured auto-ignition delay time. This deviation is negligible in some cases, but so large in other cases that the measurements must be discarded.

Such deviations have been examined and are caused by a diaphragm bursting in a finite time and by shock attenuation [1–3] due to the formation of a boundary layer, by mild ignition [4–6] and by shock–boundary interaction [7,8]. This paper focuses on mild ignition, where the ignition takes place prematurely in small spherical hot spots away from the end wall, in contrast to strong ignition, where the mixture ignites simultaneously in a volume near the end wall, which is necessary for a meaningful measurement of auto-ignition delay time. The formation of the hot spots occurs due to inhomogeneities in the flow field behind the reflected shock caused by the interaction of the reflected shock with the boundary layer. Furthermore, in many cases, the shock–boundary layer interaction leads to a bifurcation phenomenon, which has been first observed in a shock-tube experiment by Mark [7].

Communicated by D. Zeitoun and A. Higgins.

✉ J. T. Lipkowitz
timo.lipkowitz@uni-due.de
I. Wlokas
irenaeus.wlokas@uni-due.de
A. M. Kempf
andreas.kempf@uni-due.de

¹ Fluid Dynamics, IVG, University of Duisburg-Essen, Carl-Benz Straße, Duisburg, Germany

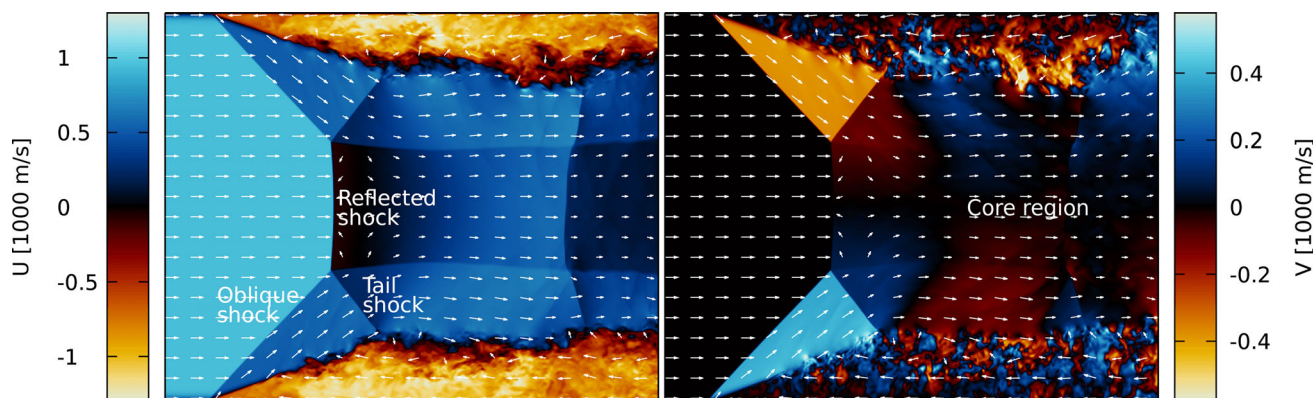


Fig. 1 Instantaneous fields of axial velocity component U (left), vertical velocity component V (right), and velocity vector field from a 3D simulation (3Db) with a grid resolution of $\Delta = 50 \mu\text{m}$

The bifurcation is characterized by a triple point connecting the reflected shock, the oblique shock, and the tail shock, as presented in Fig. 1 (left). Non-boundary-layer fluid entering the bifurcation is compressed first by the oblique shock and then by the tail shock, resulting in less entropy production and hence reduced temperatures behind the tail shock, compared to the core region. Due to the low Mach number of the fluid in the boundary layer, the pressure gradient between the undisturbed region and the boundary region behind the reflected shock reverses the boundary layer flow, resulting in a recirculation bubble. Using several simplifications, Mark [7] suggested that a bifurcation occurs if the stagnation pressure (in a shock-fixed frame) in the boundary layer is smaller than the static undisturbed pressure behind the reflected shock. Davies et al. [9] found a good agreement between their experiments and the criterion proposed by Mark, for incident Mach numbers smaller than $M = 3.6$. A bifurcation always leads to a highly non-uniform velocity field, clearing the way for mild ignition.

1.2 Mild ignition

Voevodsky and Soloukhin [10] were the first to define a criterion for mild ignition in shock tubes after several mild-ignition observations [11–13] had been made in experiments. They found a curve in the p – T plane separating the mild- and strong-ignition regimes, which was close to the curve of the upper explosion limit of H_2/O_2 mixtures. Meyer and Oppenheim [4] emphasized another criterion by relating the change in ignition delay time τ_{ig} to the change in temperature T and found a slightly better agreement for a threshold value of $\partial\tau_{\text{ig}}/\partial T = -2 \mu\text{s/K}$ compared to the first criterion. This finding demonstrates the importance of temperature fluctuations in the region behind the reflected shock and was later confirmed by one-dimensional simulations of Oran et al. [14]. They found excellent agreement regarding simulations for strong-ignition conditions and qualitative agreement in the case of mild ignition. Though one-dimensionality cannot

account for the effects of a non-uniform velocity field due to shock–boundary interaction, the numerics introduced temperature perturbations and variations in the velocity field, triggering a mild ignition. Since then, several numerical simulations [15–19] in 2D or 3D have focused on ignition behind reflected shocks in shock tubes. Oran et al. [15] presented two-dimensional simulations of ignition events in a stoichiometric ethylene–air mixture. For $M = 2.5$, strong ignition occurred, while for $M = 2.2$ mild ignition was observed. Dzieminska and Hayashi [19] observed auto-ignition behind the reflected shock in the boundary layer after the ignition occurred at the end wall. Ihme et al. [16] investigated ignition kernels in a three-dimensional simulation using an AMR (adaptive mesh refinement) code with a smallest cell size of less than $10 \mu\text{m}$. They observed ignition kernels between the tail shock and the stagnation point of the boundary layer fluid, when using adiabatic boundary conditions. Grogan et al. [17] performed 2D simulations and examined the effect of wall-boundary conditions and shock-tube diameter on ignition events. The wall-boundary condition had a significant impact on the result, since adiabatic boundary conditions resulted in mild ignition and isothermal boundary conditions in strong ignition. Additionally, a larger diameter of the shock tube led to an increased ignition delay time, providing further evidence that wall effects trigger the mild ignition. Khokhlov [18] used a 3D simulation of a stoichiometric H_2/O_2 mixture to explain the development of hot spots. The authors emphasized the role of entropy perturbations with regard to mild ignition.

1.3 Outline

In the first part of this work, the most important features and numerical methods of the LES solver are presented. Part two describes the experiment and provides basic information about the simulations and the boundary conditions. The third part presents a parameter study and examines the mild-ignition event in 3D. Temperature histories of Lagrangian

particles are used for investigating the mechanism that leads to mild ignition.

2 Numerical methods

The simulations were carried out with the LES code “PsiPhi” [20–23], using the FVM (finite volume method) approach on an equidistant, Cartesian grid, preserving the formal accuracy of the numerical schemes. In contrast to AMR methods, the high grid resolution was maintained after the shock, helping to reduce artificial numerical diffusion in the turbulent boundary layer and hence excessive numerical mixing that may strongly affect ignition. PsiPhi uses a distributed memory, domain decomposition approach for parallelization, utilizing MPI (Message Passing Interface) communication, and was run on up to 78,334 cores for the present simulations. The flow was described by the filtered conservation equations for mass, momentum, energy (1), and species (2):

$$\frac{\partial \bar{\rho} \tilde{e}_t}{\partial t} + \frac{\partial \tilde{u}_j (\bar{\rho} \tilde{e}_t + \bar{P})}{\partial x_j} = \frac{\partial \tilde{u}_j \tilde{\tau}_{ij}}{\partial x_j} - \frac{\partial \tilde{q}_j}{\partial x_j} \tag{1}$$

$$\begin{aligned} \frac{\partial \bar{\rho} \tilde{Y}_k}{\partial t} + \frac{\partial \bar{\rho} \tilde{u}_j \tilde{Y}_k}{\partial x_j} \\ = \frac{\partial}{\partial x_j} \left(\bar{\rho} \tilde{Y}_k \left[\left(D_k + \frac{\mu_t}{Sc_t} \right) \frac{\partial \tilde{Y}_k}{\partial x_j} + V_{c,k} \right] \right) + \dot{\omega}_k. \end{aligned} \tag{2}$$

The equations include the total chemical energy e_t , the tensor of frictional stresses $\tilde{\tau}_{ij}$, the diffusive flux \tilde{q}_j of energy due to heat conduction and due to species diffusion, and the correction velocity $V_{c,k}$ to ensure the conservation of mass. Further information is available from previous work [24].

$$e_t = e + \frac{u_i u_i}{2} + \sum_{k=1}^N h_{f,k}^0 Y_k \tag{3}$$

$$\begin{aligned} \tilde{q}_j = \left(\lambda + C_p \frac{\mu_t}{Pr_t} \right) \frac{\partial \tilde{T}}{\partial x_j} \\ + \bar{\rho} \sum_{k=1}^N \left(\tilde{h}_{s,k} \tilde{Y}_k \left[\left(D_k + \frac{\mu_t}{Sc_t} \right) \frac{\partial \tilde{Y}_k}{\partial x_j} + V_{c,k} \right] \right). \end{aligned} \tag{4}$$

For time-integration, a third-order low-storage Runge–Kutta scheme [25] is used and diffusive fluxes are discretized by central differencing. In order to capture shocks with minimal oscillations, the approximate Riemann solver “HR-Slau2” by Kitamura et al. [26] was used to calculate convective fluxes. The primitive quantities were interpolated to each cell face using the fifth-order, monotonicity-preserving scheme by Suresh et al. [27]. Sub-filter fluxes are modelled with eddy-viscosity and eddy-diffusivity approaches for turbulent Schmidt and turbulent Prandtl

numbers of $Pr_t = Sc_t = 0.7$. The turbulent viscosity was computed with Nicoud’s sigma model [28]. Thermochemical and transport properties, including binary diffusion coefficients, were tabulated for each species as a function of temperature using Cantera [29]. Molecular viscosity of the mixture was calculated according to the modified Wilke model [30], the mixture-averaged heat conductivity was derived using the approach of Peters et al. [31], and the mixture-averaged diffusion coefficient for species k was determined by applying the equation of Kee et al. [32]. CVODE [33,34] was used to directly solve the reaction mechanism by O’Conaire et al. [35], featuring 10 species and 40 reactions. Sub-grid modelling of the chemical source term in this context was not necessary, since the ratio of Taylor microscale to filter width was well above unity throughout the domain and more than an order of magnitude larger where the ignition occurred, i.e., in the core region. (The Taylor microscale in that context is an important length scale, since Wang and Peters found ignition kernels to be of the same order [36].)

3 Set-up

3.1 Experiment

We simulated the experiment by Meyer and Oppenheim [4] using an undiluted, stoichiometric H_2/O_2 mixture as a test gas. The pressures p_5 and temperatures T_5 behind the reflected shock were between 0.2–2.1 bar and 900–1300 K, respectively, and incident Mach numbers ranged from 2.3 to 2.9. To distinguish weak and strong ignitions, Schlieren images were taken during each experiment. The shock tube was unusual in featuring a rectangular cross section of 31.75 mm × 44.45 mm, thereby making the case particularly suitable for our high-order numerics on Cartesian grids.

3.2 Simulations

Five simulations were carried out in two dimensions to study the sensitivity of the results on grid size, numerical discretization scheme, and initial conditions. Two costly simulations (Table 1) were performed in three dimensions. To lower the computational cost, only one half of the end section (250 mm) of the rectangular shock tube was simulated for a single experiment, for which mild ignition was observed, leading to a still high computational cost of 3.8 million core hours for the largest simulation with 1.38 billion cells. Additionally, Lagrangian particles were utilized to monitor the temperature history of material (gas) particles in time.

For each main run, one or two smaller precursor simulations were required. The first one resembled the typical

Table 1 Computational grids applied for the simulations, giving the grid resolution Δ in μm , the number of cells over the length (n_i), height (n_j) and depth (n_k) of the domain, the total number of cells N (in millions), and the respective computational cost

Indication (–)	Δ (μm)	n_i (–)	n_j (–)	n_k (–)	N (10^6)	Cost (CPUh)
3Da	100	2520	315	231	183	316,800
3Db	50	4992	624	442	1377	3,760,000
2Da	100	2016	168	1	0.3	784
2Db	50	4992	315	1	1.6	7000
2Dc	25	9984	630	1	6.3	50,000
2Dd	50	4992	315	1	1.6	7000
2De	50	4992	315	1	1.6	7000

Riemann problem, simulating not only the shock, but also the rarefaction wave. At the end of the first simulation, the shock-front was located and three-dimensional profiles with approximately 10 cells before the shock-front and 50 cells behind the shock-front were stored. Those profiles contained realistic and thermodynamically compatible fields of temperature, pressure, velocities, and species and were used as initial solution in the following runs. Channel flow simulations, initialized with the state behind the incident shock and periodic inlet/outlet, were executed partly to provide inlet (the open end of the domain, opposite to the end wall) conditions and to pre-calculate the boundary layer. However, tests showed negligible differences between these inlet conditions and a zero-gradient inlet condition applied to the primitive quantities for laminar boundary layers. It is important to note that incident shock attenuation outside the computational domain was not considered at the inlet. Hence, the effect of incident shock attenuation is highly reduced in our simulations and other effects contributing to mild ignition can be investigated.

4 Results

4.1 Checking the numerical treatment in 2D

Results from tests in 2D are presented first. Figure 2 shows pseudo-Schlieren images and the ignition kernels, visualized by superimposed fields of temperature above 1100 K. To investigate the effect of grid resolution on ignition delay time τ_{ig} (defined as time until maximum temperature in the simulation exceeds 1200 K), tests were conducted in two dimensions on grids with cell sizes of 100 μm (2Da), 50 μm (2Db), and 25 μm (2Dc), yielding ignition delay times of 170 μs , 175 μs , and 177 μs , respectively, so that all grid resolutions can be seen as sufficient to simulate the auto-ignition delay time. It seems that the underlying mechanism responsible for mild ignition in the investigated case does not heavily depend on grid resolution (at least in 2D), as long as the developing boundary layer behind the incident shock is sufficiently resolved. Figure 2a–c illustrates the ignition event for the three grid resolutions. The locations of the ignition kernels appear to vary, though there is a consistent distance between

the end wall and the nearest ignition kernels, suggesting a minimum distance at which ignition will occur. Overall, all ignition kernels presented in Fig. 2 appear between 40 and 70 mm from the end wall. In addition, similarities are observed with respect to the geometry of the bifurcation and the most important shock features for the three cases.

To check the effect of the discretization, a simulation was performed with a common TVD scheme instead of the fifth-order, monotonicity-preserving scheme at a grid resolution of 50 μm (2Dd). The ignition delay time was almost as before ($\tau_{\text{ig}} = 173 \mu\text{s}$). Figure 2 shows that the result of this simulation is very similar to the solution of the higher-order scheme at medium resolution. This is the case not only for the ignition delay time, but also for the location of the ignition kernel and the most notable vortex and shock structures. One might therefore consider the improvement achieved by the higher-order scheme to be comparable to a refinement by a factor of two in each direction.

To test the impact of initial conditions, velocity perturbations were added to the initial velocity field with a standard deviation of 1 m/s. The perturbations were small and damped quickly after the start of the simulation, and one might therefore expect no change in the results. However, when comparing the second (Fig. 2b) and fifth plots (Fig. 2e) at the very same timestep, it is striking that the initial conditions had a significant effect on the locations of ignition, demonstrating a very strong sensitivity. It should be noted, however, that in the simulation without perturbations, further ignition kernels were visible shortly after and that ignition delay time was hardly affected. These observations lead to the conclusion that a meaningful simulation of the process in three dimensions is possible.

4.2 Mild ignition in 3D-LES simulations

Only three-dimensional simulations can consider realistic turbulence, but are far more expensive. Fields of the axial and vertical velocity component of the highly resolved, three-dimensional simulation (3Db) are depicted in Fig. 1 to provide a general idea of the flow fields in a bifurcated shock. Figure 3 presents instantaneous fields of pressure, temperature, and entropy as well as profiles of pressure and

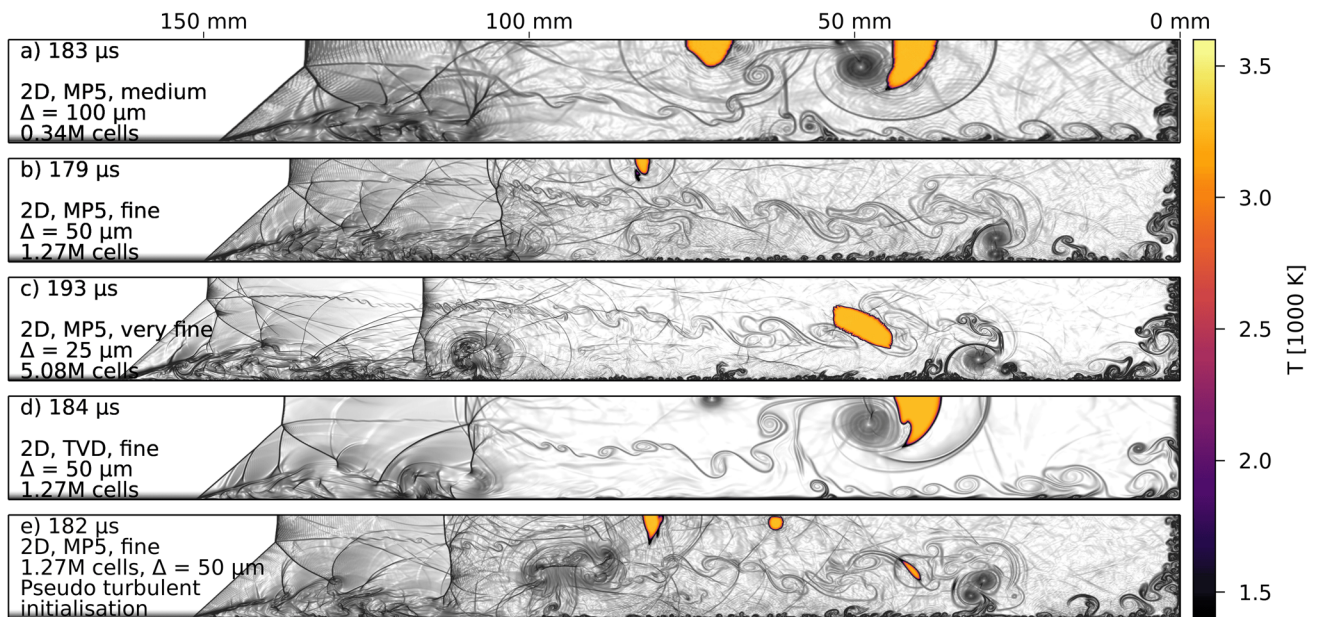


Fig. 2 Instantaneous pseudo-Schlieren images superimposed with temperature T in the two-dimensional case for different grid resolutions, discretization, and turbulent initial conditions

temperature on the centreline from the same simulation. To illustrate fields in a cross section of the shock tube, Fig. 4 presents temperature T on the left and heat release rate $\dot{\omega}_H$ on the right for the three-dimensional simulation (3Da) at a cell size of $100 \mu\text{m}$ and at a distance of 75 mm from the end wall. For convenience, the temperature field is mirrored according to the symmetry boundary condition in the middle plane. The yellow region in the plot of heat release rate indicates the location of the mild ignition.

A striking feature of Fig. 3 is the expansion region behind the normal reflected shock, followed by a second normal shock. Interestingly, the observed flow field is reminiscent of the flow downstream of an overexpanded jet, leading to the formation of a shock cell—here between the first and second normal shocks. A fine description of the flow field physics has been provided by Weber et al. [37], who did numerical investigations of reflected shock–boundary layer interaction in two dimensions with air as driven gas. The leading shock has formed the classical lambda foot so that the fluid that is adjacent to the boundary layer and that passes the oblique shock is deflected upwards. Afterwards, the fluid is compressed a second time by the tail shock, after which the static pressure equals the static pressure behind the normal reflected shock, as observed in Fig. 3. The boundary layer adjacent fluid maintains vertical momentum across the tail shock, as seen in Fig. 1, although the expansion fan behind the tail shock redirects it to the wall within a short distance. As a result, the fluid that passes the normal reflected shock is initially forced towards the centreline by the boundary layer adjacent fluid, before it “follows” the boundary layer adjacent fluid outwards. Hence, the boundary layer adjacent fluid

forms a Laval-nozzle-shaped tube around the core fluid. This is well illustrated by the slip line (in Fig. 3), which indicates the interface between the fluids that have passed through the normal and the oblique shock. Initially, when the bifurcation structure is small, the subsonic fluid (in a shock-fixed frame) is accelerated in the convergent part without reaching a Mach number of $M = 1$. Subsequently, it is compressed in the divergent part. But at some point, after the bifurcation structure grew further, the fluid in the smallest cross section of the “Laval nozzle” reaches a critical state and the supersonic fluid is further accelerated in the divergent part. Pressure waves originating from the elevated pressure reservoir at the end wall cannot travel upstream any more. As a result, a nonlinear wave forms, which finally becomes the second normal shock. Since the bifurcation structure keeps growing after the smallest cross section reached a critical value, the flow is choked and the state behind the reflected shock changes accordingly. The axial profiles (Fig. 3) of this simulated flow are well in line with the results of Weber et al. [37]. The axial profiles of temperature and pressure (Fig. 3, bottom) reveal peaks behind the normal reflected shock, which are significantly higher than the values of T_5 and p_5 , calculated by the shock tube theory of Mark [7]. While the pressure decreases monotonically with end wall distance, the temperature increases and reaches a maximum at a distance of approximately 60 mm . It is apparent that pressure and temperature are not connected by isentropic relations in this case with strong shock bifurcation. The snapshot of specific entropy s in Fig. 3 illustrates the increase in entropy with end wall distance and the entropy production resulting from the second normal shock.

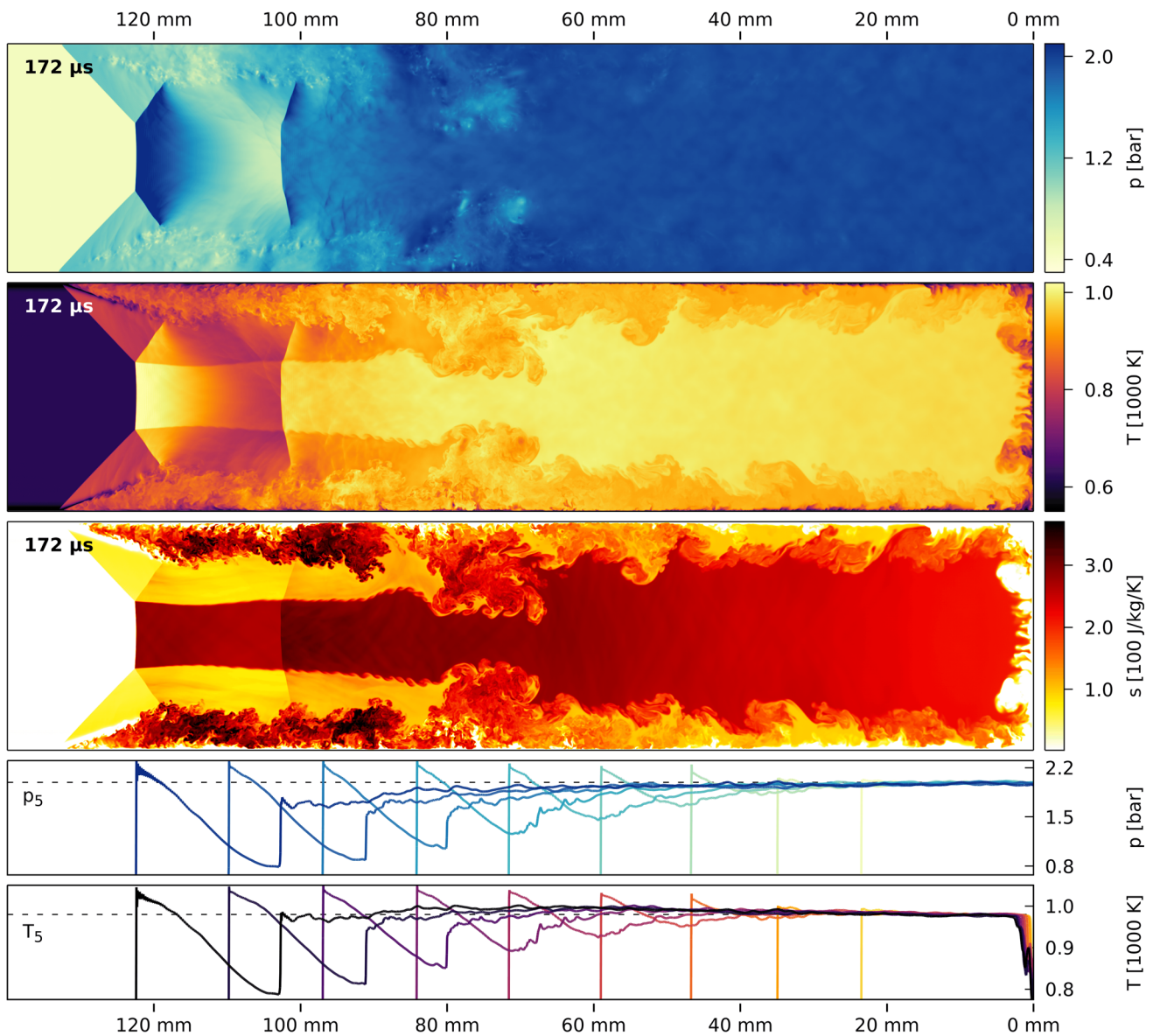


Fig. 3 Instantaneous fields of pressure p , temperature T , and specific entropy s at the top from a 3D simulation (3Db). Centreline profiles of pressure p and temperature T at the bottom coloured by respective timestep. Ignition will occur at approximately 70 mm from the end wall

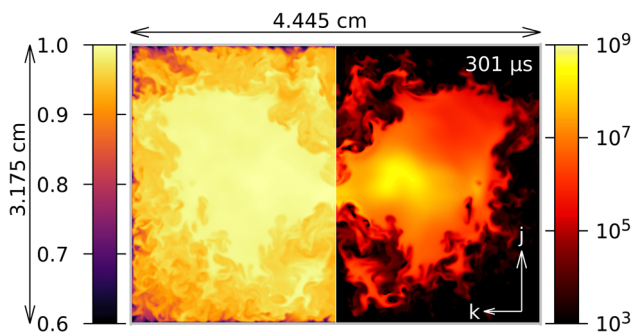


Fig. 4 Instantaneous, mirrored plot of temperature T (1000 K) on the left and instantaneous plot of heat release rate $\dot{\omega}_H$ ($\text{W}/\text{m}^3/\text{s}$) on the right in a cross section of the 3D simulation (3Da) at 75 mm from the end wall at 301 μs

Preceding 0D reactor simulations with the same reaction mechanism revealed a peak of the mass fraction of HO_2 immediately before auto-ignition. For that reason, it is a worthwhile indicator for the auto-ignition progress. Figure 5 presents the mass fraction of HO_2 shortly after ignition in the first row. It is remarkable that the HO_2 mass fraction on the centreline is up to three orders of magnitude higher than near the end wall. It is clear that mild ignition must occur near the middle plane of the shock tube, at least for this set-up. The images in the second row show the ignition region at previous timesteps, implying that local turbulent structures and temperature fluctuations might affect ignition here.

In three dimensions, an ignition delay time of 305 μs (3Da) and 256 μs (3Db) is observed, which agrees with the

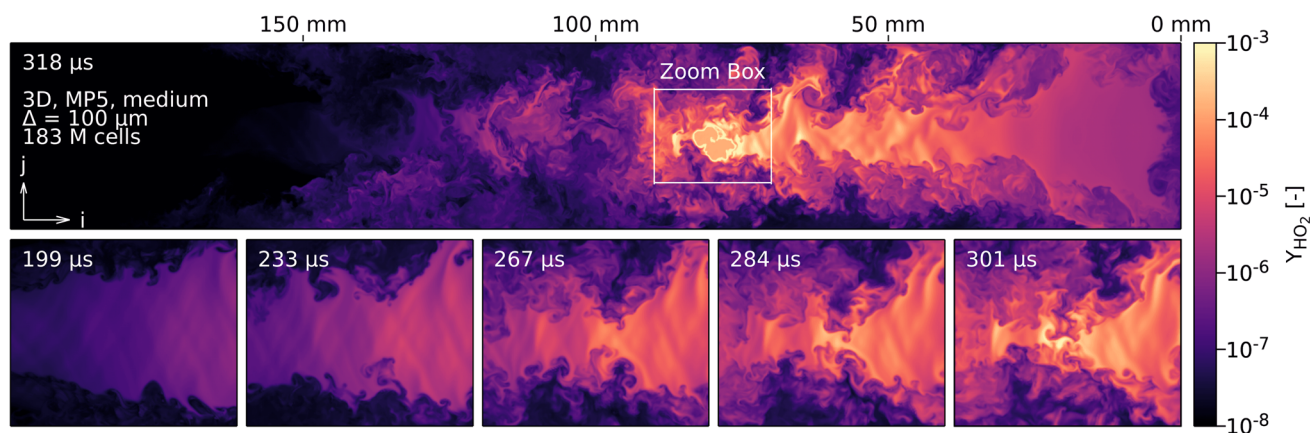


Fig. 5 Instantaneous volume-rendered fields of species mass fraction Y_{HO_2} in the 3D simulation (3Da) shortly after ignition (first row) and prior to ignition inside the zoom box (second row)

experimental evidence [4] ($250 \mu\text{s} < \tau_{\text{ig}} < 500 \mu\text{s}$) and that is much faster than the ignition delay time obtained from 0D reactor simulations, initialized with the theoretical, idealized values T_5 and p_5 (see Table 2). However, care must be taken when comparing auto-ignition delay times from simulations with those of the experiments, due to uncertainties of the reaction mechanisms at the investigated low temperatures behind the reflected shock. Auto-ignition delay times from the 2D simulations are clearly shorter than those from the 3D simulations. This is mainly caused by a less pronounced incident shock attenuation in the 2D simulations during run-time, resulting in a higher temperature behind the reflected shock of $T_5 = 985 \text{ K}$. Besides, mild ignition in 2D simulations often took place in high strain regions next to vortex structures that cannot survive in 3D, due to break-up of eddies into smaller eddies. Table 2 summarizes the auto-ignition delay time results from the simulations.

Figure 6 shows the ignition in the 3D case (3Da) by pseudo-Schlieren images superimposed with high temperatures. The “mild”-ignition kernel appears in a highly turbulent region where a detonation wave develops and quickly expands, as presented in the second row of Fig. 6, leading to a “global ignition” long before strong ignition would be expected after $1020 \mu\text{s}$. The observed wave speed is 2500 m/s , which is well in line with the theoretical result of 2600 m/s following Chapman–Jouguet theory.

4.3 Analysis with tracer particles

To investigate the temporal evolution of the thermochemical state of material fluid elements, Lagrangian tracer particles were utilized. In order to reduce the number of list entries (storing the temporal evolution of the tracked quantities), only one particle per rank was initialized after the reflected shock reached the location of the rank. This corresponds to a typical particle spacing of 1 particle/2.1 mm. The local state

was stored by the particles every few timesteps achieving a high temporal resolution. For further discussion, only certain particles were considered, which can be categorized as (i) the particle to first exceed a threshold value of $1.0\text{E}-3$ of the mass fraction of HO_2 ; this particle is labelled “Ignition particle”, and (ii) particles that were located near the *ignition particle* but closer to the end wall at the time of ignition (labelled “Closer to Endwall”), and (iii) particles that were located near the *ignition particle* but further away from the end wall at the time of ignition (labelled “Further away from Endwall”), and (iv) particles that were located in a region near the end wall at the time of ignition (labelled “Endwall-region”). The boxes in Fig. 6 indicate the three regions and the approximate location of the *ignition particle*. Particles located in the colder boundary layer near the walls ignited late and were excluded from the analysis.

Time histories of temperature and pressure are presented in Fig. 7a–c for the four particle classes. The particle data show peak temperatures and pressures significantly above the expected values of T_5 and p_5 in accordance with the axial profiles of Fig. 3. After passing the “Laval nozzle”-like flow, the temperatures of the *ignition particle* and nearby particles settle at a higher level compared to the temperature level of particles near the end wall. Figure 7b illustrates this temperature offset of the particles in more detail. Particles further away from the end wall and the *ignition particle* sensed local temperatures typically between 995 and 1000 K , while the particles closer to the end wall sensed temperatures between 985 and 995 K . This is an important observation, since higher temperatures behind the reflected shock are usually attributed to shock attenuation of the incident shock, where a subsequent change in pressure can be observed as well and be linked to the change in temperature via isentropic relations, as reported by Petersen et al. [3]. However, the effect of incident shock attenuation outside of the computational domain is not modelled at the inlet; hence, the reason for the tem-

Table 2 Auto-ignition delay times τ_{ig} from simulations and the experiment for an initial state p_5/T_5 behind the reflected shock

Indication (-)	Dimensions (-)	T_5 (K)	p_5 (bar)	τ_{ig} (μ s)	$\tau_{ig,ideal}/\tau_{ig}$ (-)
Experiment	-	980	1.80	>250	-
0Da	0	980	2.00	1020	1.00
3Da	3	980	2.00	305	3.34
3Db	3	980	2.00	256	3.98
Experiment	-	990	1.80	150	-
0Db	0	985	2.02	638	1.00
2Da	2	985	2.02	170	3.75
2Db	2	985	2.02	175	3.65
2Dc	2	985	2.02	177	3.60
2Dd	2	985	2.02	173	3.69
2De	2	985	2.02	175	3.65

Also given is the ratio of ideal ignition delay time $\tau_{ig,ideal}$ to observed ignition delay time τ_{ig} to illustrate auto-ignition delay time reduction, due to mild ignition

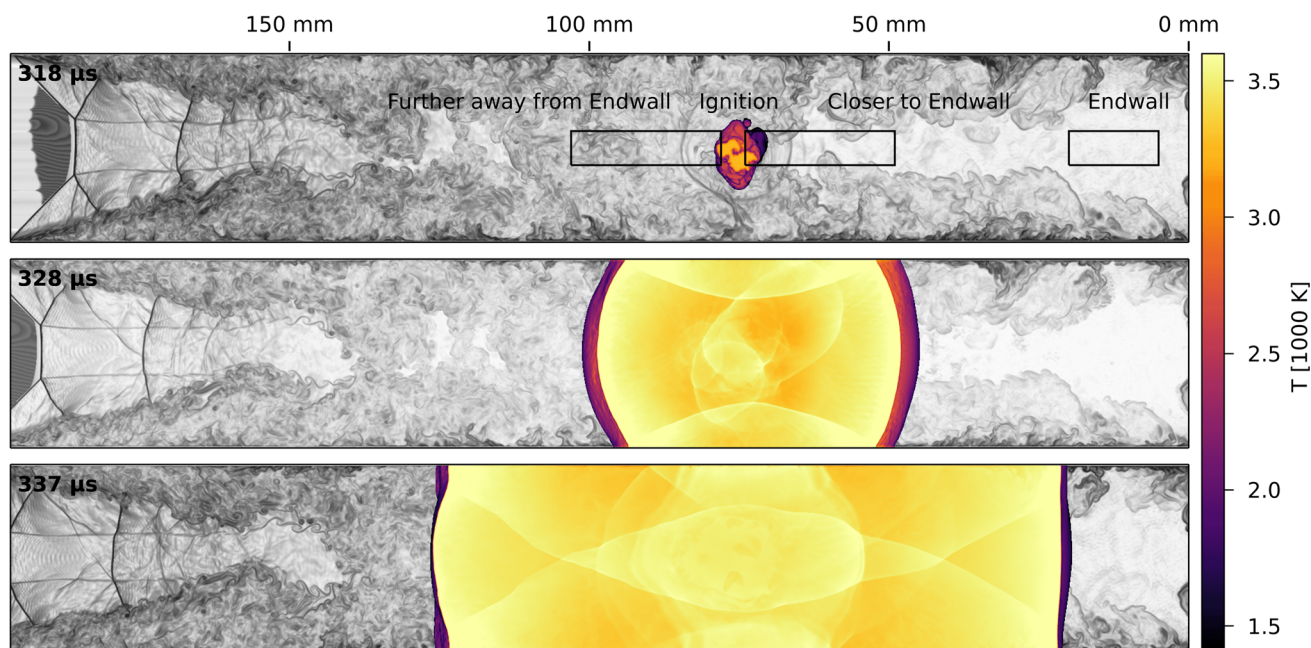


Fig. 6 Ignition in 3D (3Da). Instantaneous plots of volume-rendered pseudo-Schlieren in the background and volume-rendered temperature T above 1100 K. Rectangles indicate the regions of Lagrangian particles that are discussed in the further analysis

perature offset is likely to be different and caused by the gas dynamics behind the reflected shock. The temperature peaks of the observed particles overall increase with the distance of the particles from the end wall. However, specifically the *ignition particle* seems to reach a higher peak temperature, compared to neighbouring particles, which is also reflected in the evolution of local heat release in Fig. 7e. Here, the local heat release of the *ignition particle* is clearly greater compared to neighbouring particles. Since the second normal shock does not appear in the data of the *ignition particle*, we notice that the second shock did not trigger the ignition. Nevertheless, the ignition location is nearly identical to the location, where the second shock appeared first, at a distance

of approximately 70 mm from the end wall, as can be seen in Fig. 3.

At 125 μ s after the compression, the HO_2 concentration of the *ignition particle* exceeds that of a particle that experienced the compression 50 μ s earlier, but which is located in a slightly cooler region. This illustrates the sensitivity of auto-ignition delay time τ_{ig} with respect to temperature, which is a prerequisite for the event of mild ignition according to the criterion of Meyer and Oppenheim [4]. The temperature offset of the *ignition particle*, compared to the temperature in the vicinity of the end wall (approximately $\Delta T = 20$ K), results in higher conversion rates and is responsible for the mild ignition according to the particle data.

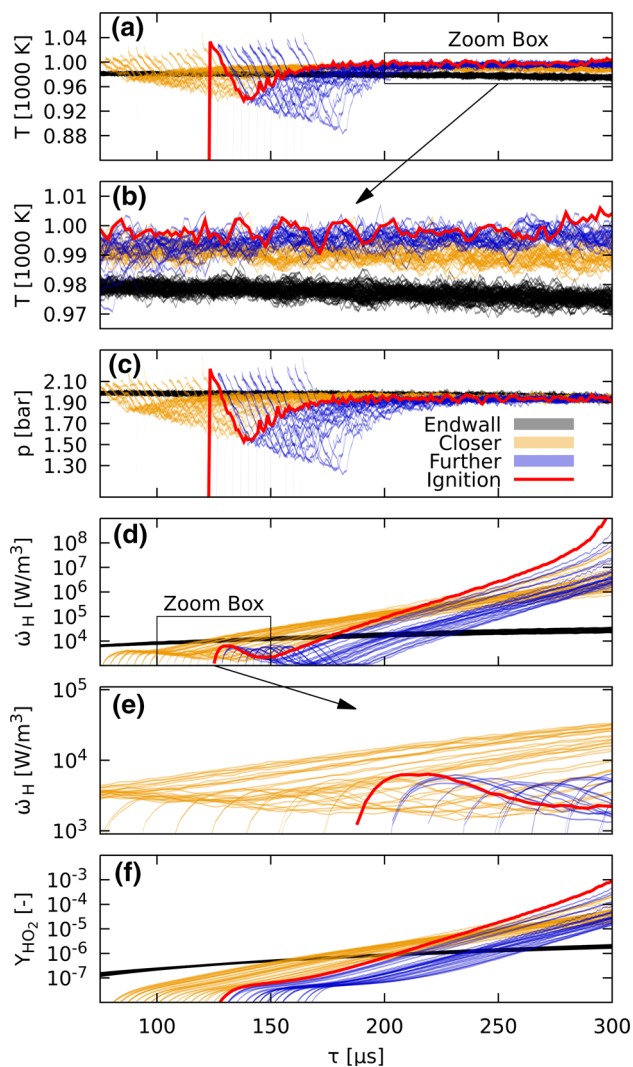


Fig. 7 Histories of temperature T , pressure p , heat release rate $\dot{\omega}_H$ ($\text{W}/\text{m}^3/\text{s}$), and species mass fraction Y_{HO_2} from Lagrangian particle data. The trajectory of the *ignition particle* is red, particles closer to the end wall are shown in orange, those further away from the end wall are shown in blue, and particles near the end wall are shown in black

Figure 8 shows the peak temperatures of the Lagrangian particles (near the centreline) and their corresponding end wall distance at peak temperature, coloured by the time of peak temperature. First, the maximum temperatures on the centreline increase with the distance from the end wall. At 110 mm, a maximum is reached after which the maximum particle temperatures decrease again. The varying temperature observed in Fig. 8 implies that the strength and speed of the reflected shock must vary, since the state is nearly constant in front of the reflected shock.

The particle data can be used to reconstruct the reflected shock-front in space and time and to compare the location to a reflected shock, travelling at constant initial speed. Figure 9 illustrates the displacement Δx between the

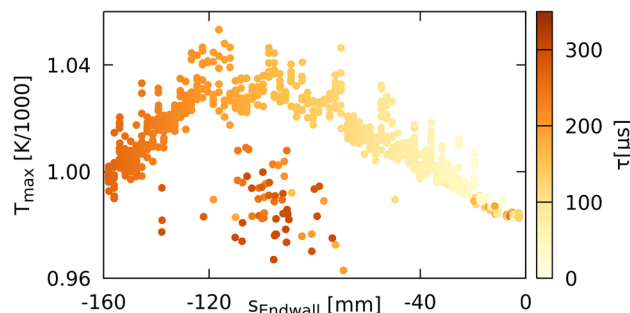


Fig. 8 Temperature peaks T_{max} of Lagrangian particles with respect to the end wall distance, coloured by time τ , after the reflection of the shock

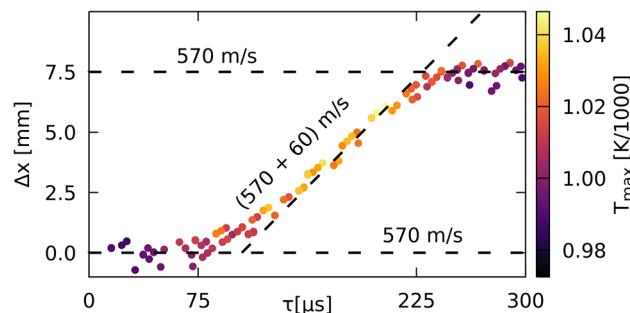


Fig. 9 Deviation Δx between position of reflected shock-front, reconstructed by Lagrangian particles, and position of shock-front at constant speed, coloured by maximum temperature T_{max} . The slope of the inflectional tangent is 60 m/s

observed reflected shock and an ideal reflected shock propagating at a constant speed of 570 m/s.

Around 100 μs after the reflection of the shock at the end wall, the shock accelerates by 60 m/s, resulting in the observed shock leading the ideal shock by 7.5 mm. The increased Mach number of the reflected shock leads to higher temperatures behind it and hence faster ignition. It appears likely that the acceleration of the shock-front is a result of the bifurcation growth. Weber et al. [37] also observed an increase in reflected shock speed in two-dimensional simulations, while Matsuo et al. [38] measured a change in reflected shock speed in their experiments.

Hot spots as a source for mild ignition have been investigated already by Lamnaouer et al. [39] in a non-reactive, axisymmetric simulation covering the whole shock tube as well as by Khokhlov [18] in a three-dimensional reactive simulation. However, Lamnaouer et al. observed hot spots in the vicinity of the end wall, travelling towards the centreline in time, which we do not observe in our set-up due to cold boundary layer fluid. Khokhlov [18], on the other hand, observed mild ignition near the corner of the shock tube, triggered by nonlinear perturbations. We noted similar mild-ignition locations at higher Mach numbers, but it is not in the scope of this paper.

Hence, this observation of varying reflected shock speed, which is consistent with previous results, enables us to link the increased speed of the reflected shock and remote ignition. We hope that our paper contributes to the understanding of such phenomena. Hanson et al. [40], for example, reported on repeatable remote ignition events at a constant distance away from the end wall, using $\text{H}_2/\text{O}_2/\text{Ar}$ mixtures at nearly the same temperature ($T_5 = 990$ K) that we had in our simulations. Interestingly, the “... exact mechanism leading to the remote ignition phenomenon is generally unknown ...” according to Hanson et al. [40].

5 Conclusions

Two-dimensional simulations and three-dimensional highly resolved large-eddy simulations of shock-tube experiments have been presented. The results emphasize the importance of the role that gas dynamic effects and turbulence play for mild ignition in shock tubes, specifically for bifurcated shocks.

The simulations in three dimensions predicted realistic ignition delay times in line with the experiment, whereas simulations in two dimensions had less incident shock attenuation during run-time, resulting in shorter ignition delay times.

The particle histories in time led to the conclusion that mild ignition results from an initial peak in temperature and a sustained offset in temperature behind the expansion region in addition to local temperature variations due to wave phenomena and turbulence. The *ignition particle* in particular was set apart from neighbouring particles by an even higher temperature.

The observed increase in temperature behind the reflected shock partially results from a “Laval-nozzle”-shaped core flow, caused by the displacement due to the bifurcation. This reflects in a varying speed of the reflected shock and is consistent with earlier observations [37,38].

Modern shock tubes have larger diameters compared to the shock tube investigated in this paper; hence, the required time until the observed flow field and the resulting effects would have an impact is significantly longer. However, since low-temperature kinetics need to be looked after, where typical ignition delay times can exceed several ms, the observed phenomena could explain ignition events far from the end wall (e.g., Fieweger et al. [41] or Hanson et al. [40]) even nowadays.

Acknowledgements The authors gratefully acknowledge the financial support by DFG Grant KE 1751/8-1, the computing time on magnitUDE granted by the Center for Computational Sciences and Simulation of the Universität of Duisburg-Essen through DFG INST 20876/209-1 FUGG, INST 20876/243-1 FUGG at the Zentrum für Informations- und Mediendienste, and the computing time on the supercomputer HazelHen

(ACID 44116). We also want to thank Elaine Oran for inspiring discussions that improved the paper.

References

1. Mirels, H.: Attenuation in a shock tube due to unsteady-boundary-layer action. NACA-TR-1333, National Advisory Committee for Aeronautics (1957)
2. White, D.R.: Influence of diaphragm opening time on shock-tube flows. *J. Fluid Mech.* **4**(6), 585–599 (1958). <https://doi.org/10.1017/s0022112058000677>
3. Petersen, E.L., Hanson, R.K.: Nonideal effects behind reflected shock waves in a high-pressure shock tube. *Shock Waves* **10**(6), 405–420 (2001). <https://doi.org/10.1007/pl00004051>
4. Meyer, J.W., Oppenheim, A.K.: On the shock-induced ignition of explosive gases. *Proc. Combust. Inst.* **13**(1), 1153–1164 (1971). [https://doi.org/10.1016/s0082-0784\(71\)80112-1](https://doi.org/10.1016/s0082-0784(71)80112-1)
5. Blumenthal, R., Fieweger, K., Komp, K.H., Adomeit, G.: Gas dynamic features of self ignition of non diluted fuel/air mixtures at high pressure. *Combust. Sci. Technol.* **123**(1–6), 1–30 (1997). <https://doi.org/10.1080/00102209708935637>
6. Chaos, M., Dryer, F.L.: Chemical-kinetic modeling of ignition delay: Considerations in interpreting shock tube data. *Int. J. Chem. Kinet.* **42**(3), 143–150 (2010). <https://doi.org/10.1002/kin.20471>
7. Mark, H.: The interaction of a reflected shock wave with the boundary layer in a shock tube. NACA-TM-1418, National Advisory Committee for Aeronautics (1958)
8. Strehlow, R.A., Cohen, A.: Limitations of the reflected shock technique for studying fast chemical reactions and its application to the observation of relaxation in nitrogen and oxygen. *J. Chem. Phys.* **30**(1), 257–265 (1959). <https://doi.org/10.1063/1.1729883>
9. Davies, L.: Influence of reflected shock and boundary-layer interaction on shock-tube flows. *Phys. Fluids* **12**(5), I–37 (1969). <https://doi.org/10.1063/1.1692625>
10. Voevodsky, V., Soloukhin, R.: On the mechanism and explosion limits of hydrogen–oxygen chain self-ignition in shock waves. *Proc. Combust. Inst.* **10**(1), 279–283 (1965). [https://doi.org/10.1016/s0082-0784\(65\)80173-4](https://doi.org/10.1016/s0082-0784(65)80173-4)
11. Berets, D.J., Greene, E.F., Kistiakowsky, G.B.: Gaseous detonations. I. Stationary waves in hydrogen–oxygen mixtures¹. *J. Am. Chem. Soc.* **72**(3), 1080–1086 (1950). <https://doi.org/10.1021/ja01159a008>
12. Fay, J.A.: Some experiments on the initiation of detonation in $2\text{H}_2\text{--O}_2$ mixtures by uniform shock waves. *Proc. Combust. Inst.* **4**(1), 501–507 (1953). [https://doi.org/10.1016/s0082-0784\(53\)80071-8](https://doi.org/10.1016/s0082-0784(53)80071-8)
13. Steinberg, M., Kaskan, W.: The ignition of combustible mixtures by shock waves. *Proc. Combust. Inst.* **5**(1), 664–672 (1955). [https://doi.org/10.1016/s0082-0784\(55\)80092-6](https://doi.org/10.1016/s0082-0784(55)80092-6)
14. Oran, E., Young, T., Boris, J., Cohen, A.: Weak and strong ignition. I. Numerical simulations of shock tube experiments. *Combust. Flame* **48**, 135–148 (1982). [https://doi.org/10.1016/0010-2180\(82\)90123-7](https://doi.org/10.1016/0010-2180(82)90123-7)
15. Oran, E.S., Gamezo, V.N.: Origins of the deflagration-to-detonation transition in gas-phase combustion. *Combust. Flame* **148**(1–2), 4–47 (2007). <https://doi.org/10.1016/j.combustflame.2006.07.010>
16. Ihme, M., Sun, Y., Deiterding, R.: Detailed simulations of shock-bifurcation and ignition of an argon-diluted hydrogen/oxygen mixture in a shock tube. 51st AIAA Aerospace Sciences Meeting including the New Horizons Forum and Aerospace Exposition Grapevine (Dallas/Ft. Worth Region), TX, AIAA Paper 2013-0538 (2013). <https://doi.org/10.2514/6.2013-538>

17. Grogan, K.P., Ihme, M.: Weak and strong ignition of hydrogen/oxygen mixtures in shock-tube systems. *Proc. Combust. Inst.* **35**(2), 2181–2189 (2015). <https://doi.org/10.1016/j.proci.2014.07.074>
18. Khokhlov, A., Austin, J., Knisely, A.: Development of hot spots and ignition behind reflected shocks in $2\text{H}_2 + \text{O}_2$. Proceedings of the 25th International Colloquium on the Dynamics of Explosions and Reactive Systems, ICDERS, Leeds, UK, Paper 020 (2015)
19. Dziemińska, E., Hayashi, A.K.: Auto-ignition and DDT driven by shock wave—boundary layer interaction in oxyhydrogen mixture. *Int. J. Hydrogen Energy* **38**(10), 4185–4193 (2013). <https://doi.org/10.1016/j.ijhydene.2013.01.111>
20. Proch, F., Kempf, A.M.: Numerical analysis of the Cambridge stratified flame series using artificial thickened flame LES with tabulated premixed flame chemistry. *Combust. Flame* **161**(10), 2627–2646 (2014). <https://doi.org/10.1016/j.combustflame.2014.04.010>
21. Rittler, A., Deng, L., Wlokas, I., Kempf, A.: Large eddy simulations of nanoparticle synthesis from flame spray pyrolysis. *Proc. Combust. Inst.* **36**(1), 1077–1087 (2017). <https://doi.org/10.1016/j.proci.2016.08.005>
22. Rieth, M., Proch, F., Rabaçal, M., Franchetti, B., Marincola, F.C., Kempf, A.: Flamelet LES of a semi-industrial pulverized coal furnace. *Combust. Flame* **173**, 39–56 (2016). <https://doi.org/10.1016/j.combustflame.2016.07.013>
23. Nguyen, T., Kempf, A.M.: Investigation of numerical effects on the flow and combustion in LES of ICE. *Oil Gas Sci. Technol.* **72**(4), 25 (2017). <https://doi.org/10.2516/ogst/2017023>
24. Poinso, T.J., Veynante, D.: Theoretical and Numerical Combustion, 3rd edn. Aquaprint, Bordeaux (2012)
25. Williamson, J.: Low-storage Runge–Kutta schemes. *J. Comput. Phys.* **35**(1), 48–56 (1980). [https://doi.org/10.1016/0021-9991\(80\)90033-9](https://doi.org/10.1016/0021-9991(80)90033-9)
26. Kitamura, K., Hashimoto, A.: Reduced dissipation AUSM-family fluxes: HR-SLAU2 and HR-AUSM⁺-up for high resolution unsteady flow simulations. *Comput. Fluids* **126**, 41–57 (2016). <https://doi.org/10.1016/j.compfluid.2015.11.014>
27. Suresh, A., Huynh, H.: Accurate monotonicity-preserving schemes with Runge–Kutta time stepping. *J. Comput. Phys.* **136**(1), 83–99 (1997). <https://doi.org/10.1006/jcph.1997.5745>
28. Nicoud, F., Toda, H.B., Cabrit, O., Bose, S., Lee, J.: Using singular values to build a subgrid-scale model for large eddy simulations. *Phys. Fluids* **23**(8), 085106 (2011). <https://doi.org/10.1063/1.3623274>
29. Goodwin, D.G., Moffat, H.K., Speth, R.L.: Cantera: An Object-oriented Software Toolkit for Chemical Kinetics, Thermodynamics, and Transport Processes. Version 2.4.0 (2017). <https://doi.org/10.5281/zenodo.170284>
30. Bird, R.B., Stewart, W.E., Lightfoot, E.N.: Transport Phenomena. Wiley, New York (1960)
31. Peters, N., Warnatz, J. (eds.): Numerical Methods in Laminar Flame Propagation. Vieweg+Teubner Verlag, Braunschweig (1982). <https://doi.org/10.1007/978-3-663-14006-1>
32. Kee, R.J., Coltrin, M.E., Glarborg, P.: Chemically Reacting Flow. Wiley, New York (2003). <https://doi.org/10.1002/0471461296>
33. Cohen, S.D., Hindmarsh, A.C., Dubois, P.F.: CVODE, a stiff/nonstiff ODE solver in C. *Comput. Phys.* **10**(2), 138 (1996). <https://doi.org/10.1063/1.4822377>
34. Hindmarsh, A.C., Brown, P.N., Grant, K.E., Lee, S.L., Serban, R., Shumaker, D.E., Woodward, C.S.: SUNDIALS: Suite of nonlinear and differential/algebraic equation solvers. *ACM Trans. Math. Softw.* **31**(3), 363–396 (2005). <https://doi.org/10.1145/1089014.1089020>
35. Conaire, M.Ó., Curran, H.J., Simmie, J.M., Pitz, W.J., Westbrook, C.K.: A comprehensive modeling study of hydrogen oxidation. *Int. J. Chem. Kinet.* **36**(11), 603–622 (2004). <https://doi.org/10.1002/kin.20036>
36. Wang, L., Peters, N.: The length-scale distribution function of the distance between extremal points in passive scalar turbulence. *J. Fluid Mech.* **554**(1), 457–475 (2006). <https://doi.org/10.1017/s0022112006009128>
37. Weber, Y.S., Oran, E.S., Boris, J.P., Anderson, J.D.: The numerical simulation of shock bifurcation near the end wall of a shock tube. *Phys. Fluids* **7**(10), 2475–2488 (1995). <https://doi.org/10.1063/1.868691>
38. Matsuo, K., Kawagoe, S., Kage, K.: The interaction of a reflected shock wave with the boundary layer in a shock tube. *Bull. JSME* **17**(110), 1039–1046 (1974). <https://doi.org/10.1299/jsme1958.17.1039>
39. Lamnaouer, M., Kassab, A., Divo, E., Polley, N., Garza-Urquiza, R., Petersen, E.: A conjugate axisymmetric model of a high-pressure shock-tube facility. *Int. J. Numer. Methods Heat Fluid Flow* **24**(4), 873–890 (2014). <https://doi.org/10.1108/hff-02-2013-0070>
40. Hanson, R.K., Pang, G.A., Chakraborty, S., Ren, W., Wang, S., Davidson, D.F.: Constrained reaction volume approach for studying chemical kinetics behind reflected shock waves. *Combust. Flame* **160**(9), 1550–1558 (2013). <https://doi.org/10.1016/j.combustflame.2013.03.026>
41. Fieweger, K., Blumenthal, R., Adomeit, G.: Self-ignition of S.I. engine model fuels: A shock tube investigation at high pressure. *Combust. Flame* **109**(4), 599–619 (1997). [https://doi.org/10.1016/s0010-2180\(97\)00049-7](https://doi.org/10.1016/s0010-2180(97)00049-7)

Publisher's Note Springer Nature remains neutral with regard to jurisdictional claims in published maps and institutional affiliations.